UNIVERSITY OF CRETE
SCHOOL OF SCIENCES AND ENGINEERING

DEPARTMENT OF PHYSICS

Effect of hydroxyapatite nanoparticles in an alginate-gelatin bioink for bone tissue engineering applications

Bachelor Thesis

Nikolaos Koutsomarkos

Supervisor: Associate Professor Maria Chatzinikolaidou

HERAKLION

OCTOBER 2021

Abstract

3D bioprinting utilises a 3D printing technique with the addition of cells within the printed construct. It has grown rapidly, in recent years, with many applications in cartilage and bone formation while testing a plethora of material-candidates for a specific application. Some well-studied candidates are blends of Alginate - Gelatin (Alg - Gel) which provide excellent printability and biocompatibility though there is little research on a blend of Alg - Gel with nanohydroxyapatite particles (nHA). In this work, six blends of 7% w/v Alg - 8% w/v Gel with varying percentage of nHa from 0% to 5% were studied through their printing accuracy, their printability using rheological studies and their water content and the effect of the addition of nHA particles was assessed. An optimal blend was chosen by these factors and was studied further by conducting a cell viability test.

Acknowledgments

I would like to express my sincere gratitude to Prof. Maria Chatzinikolaidou for her deep trust that she placed in me. Her enthusiastic motivation and her patient guidance were detrimental for my work and she has helped me to go further and beyond. I profoundly appreciate the opportunity that she gave me to work in her group on the field of biomaterials and tissue engineering and I am forever grateful that she introduced me to this field.

I would be remiss not to mention Prof. Dimitris Vlassopoulos and Katerina Peponaki for their help and meaningful conversations on the rheology measurements and results.

I would also like to thank Dr. Elena Deligianni for our helpful discussions and the imaging and quantification of cell viability.

Many thanks to Danai, Georgianna, Konstantinos and Varvara for their endless support and conversations throughout my time in the lab.

Finally, I would like to thank my friends and family for their support and encouragement.

Contents

1. Introduction

1.1. Biomaterials

A biomaterial is a material intended to interface with biological systems to evaluate, treat, augment or replace any tissue, organ or function of the body [7]. Thus, biomaterials science is the study (from the physical and/or biological perspective) of biomaterials with specific reference to their interaction with the biological environment. Emphasis in the biomaterials field has been on synthesis, characterization and the host-material interactions biology [8]. Because the final goal of the field is the development of materials that will be implanted in humans, one of the most important concepts in biomaterials science is that of biocompatibility, which refers to the ability of a material to perform with an appropriate host response in a specific application[7, 9]. Examples of "appropriate host responses" include, resistance to blood clotting, resistance to bacterial colonization and normal, uncomplicated healing. Examples of "specific applications" include a hemodialysis membrane, a urinary catheter or a hip joint replacement prosthesis [8]. Generally, materials are classified as organic if they contain carbon or inorganic if they do not. Specifically, biomaterials fall into one of four categories of materials: metals, ceramics, polymers and their combination (composites) [9, 10]. Table 1 lists a few applications for biomaterials in the body and gives estimates of the specific device global market size and, where available, an estimate of the number of medical devices utilized annually.

1.2. Tissue engineering

Tissue and organ failure due to disease, injury and developmental defects has become a major economical and healthcare concerns [11]. Nowadays, use of donated tissues and organs is the clinical practice to address this situation. However, due to the shortage of organ donors, the increasing number of people on the transplant waiting lists and an ever-increasing aging population, dependence on donated tissues and organs is not a practical approach [3]. In the United States alone, more than 117.000 people are on the national transplant waiting list and more than 15.000 people have been waiting for more than 5 years for a transplant (US Department of Health and Human Services, Organ Procurement and Transplantation network; https://optn.transplant.hrsa.gov/; data as of October, 2021). Tissue engineering and regenerative medicine are multidisciplinary fields that apply principles of engineering and life sciences toward the development of biological substitutes that restore, maintain and improve the function of damaged tissues and organs. As a multidisciplinary science, tissue engineering merges the fields of biology, material science, chemistry, engineering and medicine to fabricate new functional tissue using living cells combined with a specific biomaterial [12].

Application	Biomaterials Used	Number per Year – Global (Global Market in US$)
Skeletal System		
Joint replacements (hip, knee, and shoulder)	Titanium, CoCr, polyethylene, alumina, zirconia	4,000,000 ($16B)
Trauma fixation devices (plates, screws, pins, and rods)	Titanium, stainless steel, CoCr, polyether ether ketone, poly(lactic acid) (PLA)	1,500,000 ($5.5B)
Spine disks and fusion hardware	Nitinol, titanium, polyether ether ketone, stainless steel	1,100,000 ($8.5B)
Bone cement (fixation)	Polymethyl methacrylate (PMMA), glass polyalkenoate (ionomer), calcium phosphate cements	($1.1B)
Cartilage, tendon, or ligament repair and replacement	Decellularized porcine tissue, poly(lactide) and metallic fixation devices, collagen, hyaluronic acid lubricants	($8.6B)
Dental implant-tooth fixation	Titanium, zirconium	10,000,000 ($4B)
Cardiovascular System		
Vascular grafts, patches, and endovascular devices (stent grafts)	Dacron, expanded poly(tetrafluoroethylene), Nitinol, CoCr, stainless steel, fixed tissue	($2.5B)
Application	Biomaterials Used	Number per Year – Global (Global Market in US$)
Heart valves: mechanical and bioprosthetic (transcatheter and traditional)	Dacron, carbon, CoCr, fixed bovine and porcine tissue, stainless steel, Nitinol	600,000 ($5.5B)
Pacemakers	Titanium, polyurethane	1,000,000 ($6.5B)
Stents: coronary, peripheral vasculature, and nonvascular	Stainless steel, Nitinol, CoCr, Pt, tantalum, Mg alloys, poly(styrene-b-isobutylene-b-styrene), poly(n-butyl methacrylate), polyethylene-co-vinyl acetate, phosphoryl choline containing block copolymers, poly(lactic-co-glycolic acid), PLA	5,000,000 ($10.6B)
Catheters: cardiovascular, urologic, and others	Polytetrafluoroethylene (PTFE), poly(vinyl chloride), silicone, polyurethane	($28B)
Organs		
Hemodialysis	Polysulfone, modified cellulose, polyacrylonitrile, polycarbonate, silicone, polyvinylchloride	2,000,000 patients ($12B)
Skin substitute (chronic wounds, burns)	Collagen, cadaver skin, alginate, polyurethane, carboxymethylcellulose, nylon, silicone	($1.3B)
Ophthalmologic		
Contact lens	PMMA, polyhydroxyethylmethacrylate (PHEMA), polyvinyl alcohol, polyvinyl pyrrolidone, silicone (polydimethyl siloxane [PDMS])	($7.5B)
Other		
Cochlear prostheses	Platinum, platinum–iridium, PDMS, titanium, aluminum oxide	45,000 ($2.7B)
Breast implants	PDMS	3,600,000 ($1.2B)
Sutures	Silk, nylon, poly(glycolic acid), PLA, polydioxanone, polyester copolymers, polypropylene, PTFE, processed bovine tissue	($3.9B)
Blood bags	Poly(vinyl chloride)	($170M)

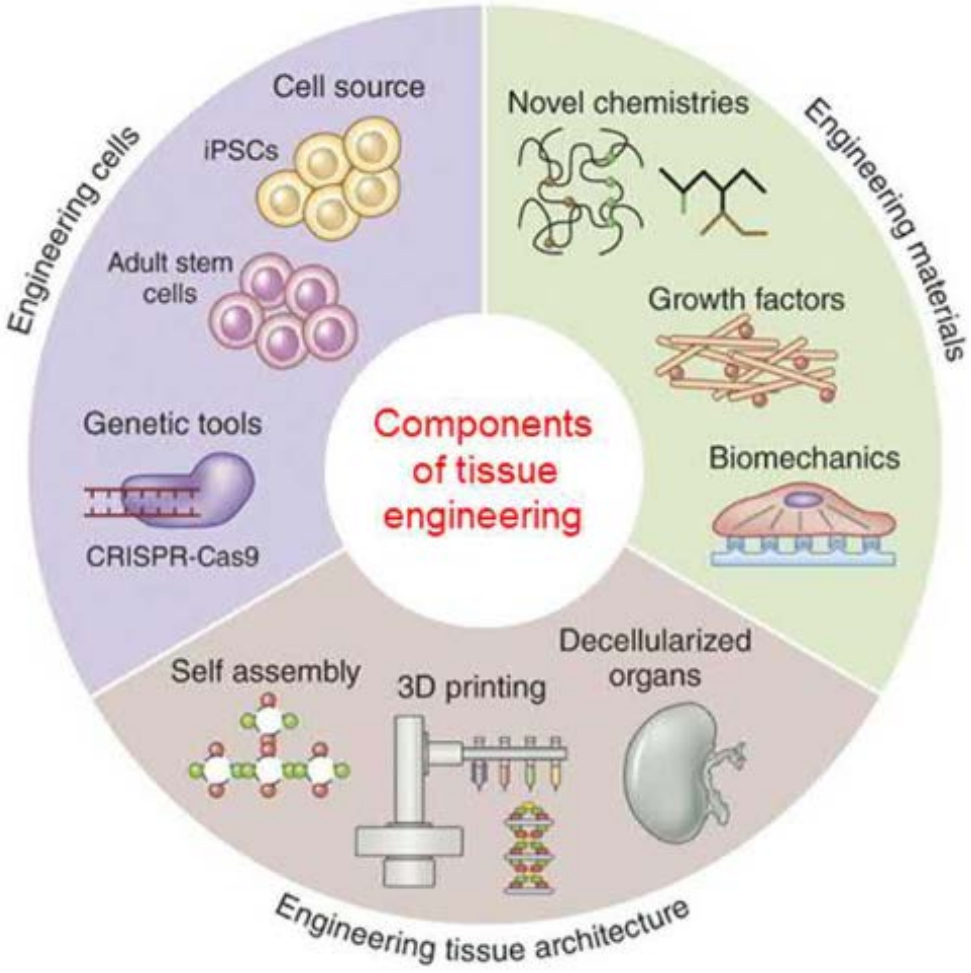

Figure 1 Schematic representation of different aspects of tissue engineering. Each component (materials, cells and tissue architectures) can be engineered separately or in combination to achieve the therapeutic goals [3].

1.3. Bioprinting

Bioprinting is a relatively new field that uses a computer-controlled three-dimensional (3D) printing device to accurately deposit cells either alone or mixed with biomaterials (bioink) into precise geometries with the goal being the creation of anatomically correct biological structures for tissue engineering and regenerative medicine purposes. A number of bioprinting approaches have been recently explored, encompassing the use of extrusion devices, inject-like printers and laser-assisted devices [13]. The most common printing techniques which are currently being employed are extrusion-based deposition, inkjet bioprinting, stereolithography and laser-induced forward transfer (LIFT) [14]. In a typical extrusion-based bioprinter the bioink is loaded into a syringe barrel and is extruded through a micro-nozzle tip either using pneumatic pressure or by mechanical force by means of a piston or screw [15, 16]. Inkjet bioprinting is achieved by using the drop on demand system in which droplets are ejected only when and where actuation occurs, thus enabling the precise spatiotemporal control [16]. Similarly to extrusion-based bioprinting,

the bioink is loaded in a cartridge which is connected to a micro-nozzle tip. During printing, the ink in the cartridge is displaced by a controlled pressure pulse. Once the pulse energy exceeds the threshold, a droplet is ejected from the nozzle [17]. Stereolithography techniques utilize photochemical processes in which light (typically UV or near-UV) causes monomers in a reservoir to polymerize into 3D networks in a layer-by-layer fashion by selective polymerization [16]. Fabrication occurs at the surface of the reservoir and the stage lowers incrementally, allowing layers to be polymerized on top of each other, therefore creating 3D structures [18]. The LIFT setup consists of a laser source, a focusing system, a donor ribbon, which is a solid plate transparent to the laser wavelength coated with an energy absorbing layer and a bioink, and a collector substrate. The laser beam generates a high pressure vapor bubble that pushes the bioink forward and the resulting jet or droplet lands on the collector substrate [19]. Table 2 shows the advantages, limitations, minimum resolution capabilities and print speeds of the bioprinting techniques mentioned above.

Table 2. Comparison between bioprinting techniques, adapted from [16]

Technique	Advantages	Limitations	Minimum Resolution	Speed
Extrusion	-low cost/ease of use -wide range of hydrogels -modular capabilities -scalability -high cell density	-limited resolution -nozzle clogging -limited print rate -shear thinning properties of hydrogels	~100 µm	0.01-20 mm/s
Inkjet	-reduced nozzle clogging -high cell density -large-scale surfaces -economical, scalable	-limited viscosity range -limited total volumes -high shear stresses -cell sedimentation	~20-100 µm	10.000 droplets per second
Stereolithography	-high resolution -relatively high speed -structure strength	-limited hydrogel selection due to viscosity restrictions -requirement of support structures -layer by layer curing (anisotropy)	~10-20 µm	700 mm/h
LIFT	-high resolution, pL size droplets -print feature complexity -high cell density -high biocompatibility	-impractical for large structures, expensive -small print volumes -cell sensitivity to laser irradiation -metallic nanoparticle leaching	~10-20 µm	200-1600 mm/s

1.4. Bone tissue engineering

1.4.1. Bone

The skeletal system performs vital functions: support, movement, protection, blood cell production, calcium storage and endocrine regulation [20]. Bone is a composite material consisting of apatite mineral, organic matrix, cells and water. Specifically, the apatite mineral is considered to be a carbonated apatite ($Ca_5(PO_4CO_3)_3$) similar to hydroxyapatite

(as described in section 2.7.) and provides the bone stiffness and strength. Type I collagen protein is the main constituent of the organic matrix (more than 90%) and supplies the bone with strength and flexibility. The other constituents of the organic matrix are non-collagenous proteins such as osteocalcin, osteonectin and osteopontin which may influence the events associated with bone remodelling which includes the recruitment, attachment, differentiation and activity of bone cells [21]. Bone cells fall into three cell types: osteoblasts, osteoclasts and osteocytes. Osteoblasts are responsible for bone formation, osteoclasts for bone resorption and osteocytes for cell-to-cell communication with all bone cells. When in balance, the remodelling process of the bone involves equal and linked participation of both osteoclasts and osteoblasts [22].

1.4.2. Necessity of tailored bone implants

The lifetime risk for sustaining a fracture in the wrist, hip or vertebrae is estimated to be between 30% and 40% of the total population, in developed countries. Under most circumstances, fractures in bone will heal naturally, however there are conditions that require intervention such as fractures that fail to heal and chronic conditions such as osteoporosis [23]. Current state-of-the-art prosthetic implants fail to meet structural and functional requirements that would render them as permanent remediation solutions. As a result, patients undergo painful and costly subsequent surgeries for implant replacements or readjustments [24]. The ultimate goal of bone tissue engineering is a creation of the bone graft substitute [25]. 3D printing technologies have made it possible to tailor bone implants to the individual trauma site. This is a huge advance in the field of personalized medicine and it can make a big impact in areas like reconstructive surgery, where physical appearance is a very important factor in the treatment success [23].

1.5. Alginate

Alginate is isolated from brown algae (class Phaeophyceae) of the following genera *Ascophyllum, Durvillaea, Ecklonia, Laminaria, Lessonia, Macrocystis* and *Saccharina* and it's typically extracted by following five steps: acidification of the algae, alkaline extraction with sodium carbonate (Na_2CO_3), solid/liquid separation, precipitation and drying [2, 26]. Alginate is a linear, unbranched block copolymer composed of variable ratio of β-D-mannuronic acid (M) and α-L-guluronic acid (G) bonded by 1 → 4 glycosidic bonds. The copolymer blocks are either consecutive (i.e., MMMM or GGGG) or alternating (i.e., MGMG) and the relative amount of the blocks and the M/G ratio depend upon the source of the alginate [27]. Sodium alginate is soluble in water and alkaline solutions, but it's insoluble in hydroalcoholic solutions, in which the alcohol content is greater than 30% w/v, in organic solvents such as chloroform and ether, and in acids with pH lower than 3.0 [28]. Hydrogel formation of sodium alginate is achieved by exposure to divalent cations such as Ca^{2+}, Sr^{2+} and Ba^{2+}. Of these, Ca^{2+} ions are most commonly used as they are innate to the human body. Mg^{2+} ions do not induce gelation while Pb^{2+}, Cu^{2+}, Cd^{2+}, Co^{2+}, Ni^{2+}, Zn^{2+} and Mn^{2+} are generally toxic. The crosslinking of the copolymer is achieved by the exchange of sodium ions from the G blocks with the divalent cations and the stacking of these G blocks to form

an egg-box structure as shown in Figure 2 [29, 30]. The viscosity of alginate is dependent on its concentration, its molecular weight and the pH of the solution. Alginates formed from high molecular weight are more viscous than those from low molecular weight and as the pH of the alginate solution decreases, the viscosity increases, reaching a maximum around pH 3-3.5 [1]. Mammalian cells do not possess receptors for alginate polymers and therefore alginate constructs do not promote significant cell adhesion [31]. Despite that, sodium alginate is biocompatible, nonimmunogenic (does not provoke an immune response), noncytotoxic (not toxic to cells) and biodegradable and due to these properties, it has been used in bioprinting either alone or combined with other materials for multiple tissue engineering applications such as bone, nerve, eye, ear, skin, tooth, cartilage, heart and liver [32-42].

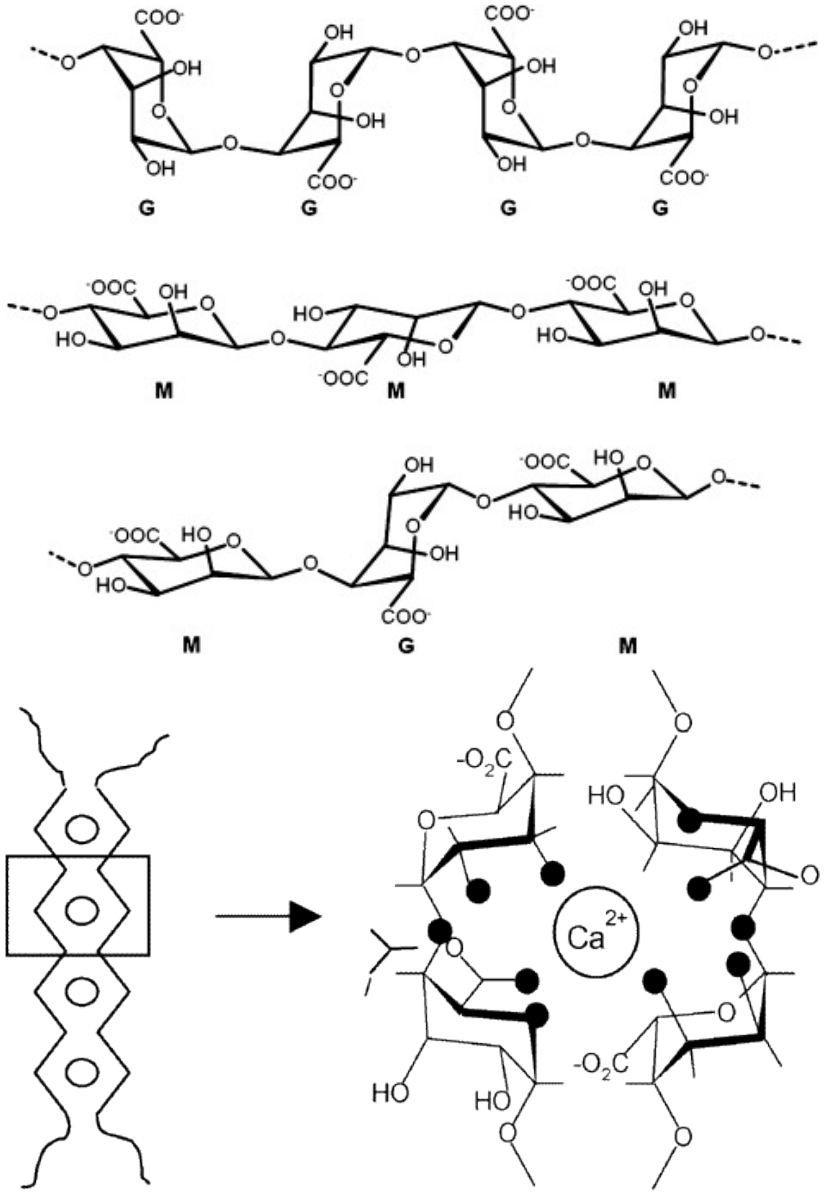

Figure 2 Alginate structure and the egg-box model[1, 2]

1.6. Gelatin

Gelatin is a denatured polypeptide derived from the controlled partial hydrolysis of collagen, which is found abundantly in nature and is the major constituent of skin, bones and connective tissue [43]. Structurally, gelatin molecules contain repeating sequences of Glycine-X-Y triplets, where X and Y are usually proline and hydroxyproline amino acids.[44] The main sources of gelatin are porcine, bovine and fish skin and along with the type of collagen that's derived from (mainly I, IV) and the manufacturing process, they crucially affect its characteristics [45]. The crosslinking of gelatin is essential for biomedical applications since it's soluble in aqueous solutions at temperatures above 30 ^{o}C. Among the chemical crosslinking agents such as glutaraldehyde (GTA), dextran dialdehyde and genipin, GTA is by far the most frequently used [46]. The crosslinking mechanism involves the reaction of free amino groups or amino acid residues of the polypeptide chains with the aldehyde groups of GTA [47]. The mechanical properties of gelatin heavily depend on the crosslinking process. By varying the concentration of gelatin and crosslinking parameters, it is possible to adjust the mechanical properties of the gelatin construct [45]. However, that is limited as gelatin lacks thermal stability and has relatively high degradation rate and therefore it's common to modify gelatin or combine it with other materials to improve the mechanical stability and bioactivity [48]. The frequent use of gelatin stems due to the fact that it is biocompatible, fully absorbable biopolymer, promotes cell proliferation and contains abundant motifs such as arginine-glycine-aspartic (RGD) sequences, which are a recognition sequence for integrin-mediated cell adhesion [44, 49]. Due to these properties, gelatin (usually chemically modified) in synergy with other biomaterials, is favored for a bioink formulation for myriad tissue engineering applications like neural, skin, cartilage,

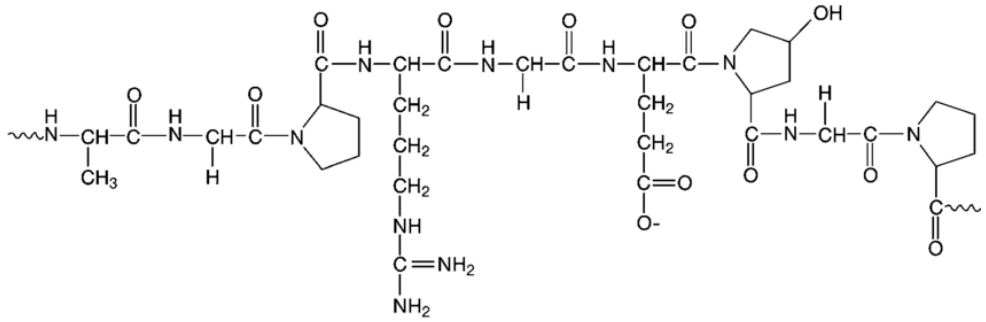

Figure 3 Chemical structure of gelatin [4]

bone, heart and eye. [49-55]

1.7. Hydroxyapatite

Hydroxyapatite (HA) ($Ca_{10}(PO_4)_6(OH)_2$) is an inorganic component found in bones and teeth and is characterized with a hexagonal crystallographic structure, as shown in Figure 4. Specifically, PO_4^{3-} moieties are arranged such that four Ca^{2+} atoms are surrounded

by nine O^{2-} atoms of the PO_4^{3-} moieties, while the other six Ca^{2+} atoms are surrounded by the remaining six atoms of the PO_4^{3-} moieties [56]. Pure HA has the stoichiometric Ca to P ratio of 1.67 and lattice parameters: a-axis = 0.9422 nm, c-axis = 0.688 nm [57]. HA is similar to bone in composition and is bioactive (able to directly bond to bone, thus forming a uniquely strong interface), osteoconductive (able to serve as a template or guide for the newly forming bone) and combined with mesenchymal stem cells can be osteoinductive (able to induce de novo bone formation) [58, 59]. Usually nanoparticles of HA are added to a polymer solution in order to mimic the bone composition which is approximately 75 inorganic to 25 organic by weight and 65 to 35 by volume [57]. When used in bioprinting for cartilage and bone tissue engineering it has been shown that it improves the stability and

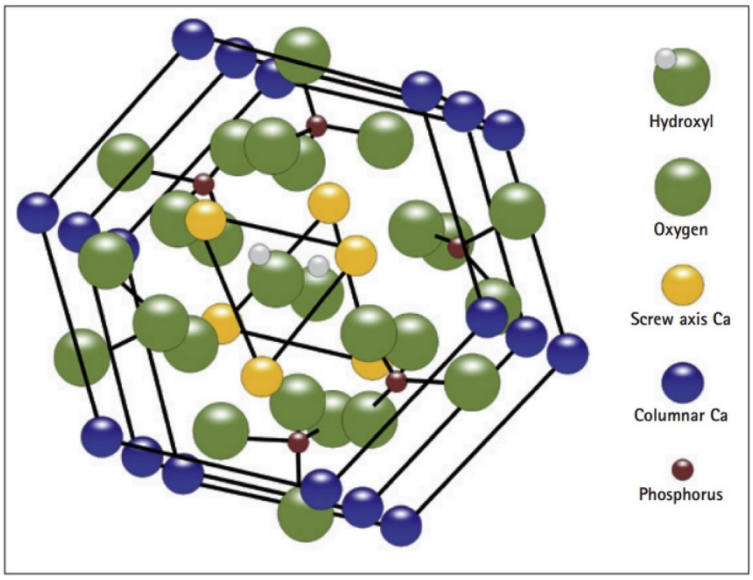

Figure 4. Illustration of the structure of hydroxyapatite [6].

mechanical strength of the construct and the printing accuracy, while also it can augment the viability and proliferation of cells [60-63].

2. Materials and Methods

2.1. Preparation of Alginate-Gelatin-Hydroxyapatite hydrogel

Briefly, for 10 ml 7%Alg-8%Gel-3%nHA blend, 2 ml of hydroxyapatite paste (nanoXIM·Care Paste, FLUIDINOVA, S.A., Maia, Portugal) was dissolved in ultrapure water or 1x PBS and stirred for 10 min at 70 ^{o}C. Then, 0.8 g gelatin (Gelatin, type B from bovine skin, Sigma-Aldrich, USA) was added and mixed for 15 min (until it was completely dissolved). Finally, 0.7 g of alginate (Alginic acid sodium salt from brown algae, medium viscosity, Sigma-Aldrich, UK) was incorporated into the solution and stirred for 2 h. The hydrogels for every experiment were kept at 4 ^{o}C until use and were only heated to the desired temperature as they exhibit thermal hysteresis [64].

2.2. Fourier-transformed infrared spectroscopy

Fourier-transformed infrared spectroscopy (FTIR) is a technique which obtains an infrared spectrum from the testing sample. Infrared spectra are a result from transitions between quantized vibrational energy states. The number of ways that the atoms can vibrate are called vibrational modes and every molecule has a slightly different vibrational mode from all other molecules. Therefore, the infrared spectrum of a given molecule is unique and can be used to identify that specific molecule [65]. FTIR analysis of pure materials and all blends was performed by means of an optical spectrometer (Nicolet 6700, Thermo Fisher Scientific) within the wavenumber region 500–4000 cm^{-1}. The spectral data were collected and the numerical values were transferred to Origin software for graphical presentation.

2.3. Rheology

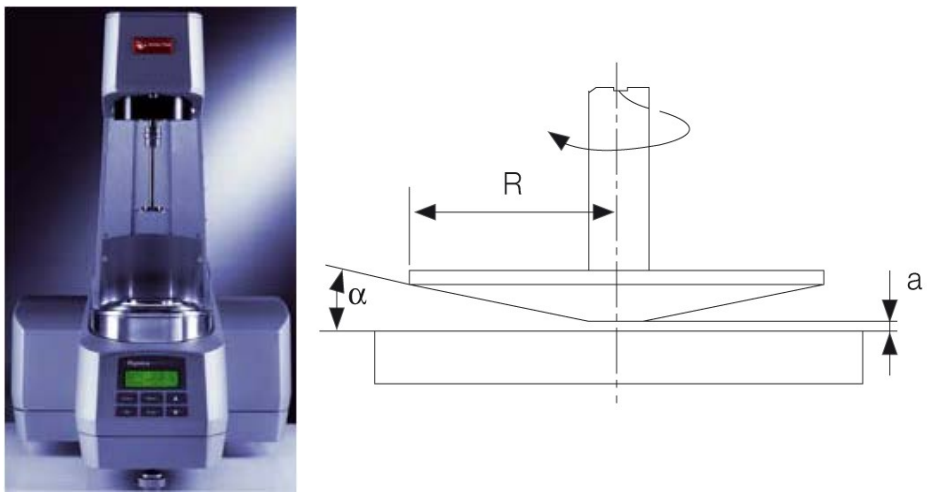

Figure 5. The MCR501 rheometer (left) and the cone-plate geometry (right).

The comprehension of the flow behaviour of the material-candidate is fundamental for extrusion based bioprinting. The study of flow and deformation of matter is the subject of rheology [66]. A rotational rheometer measures or applies torque, angular displacement and angular velocity and calculates shear stress, shear strain and shear strain rate. All rheological measurements were performed with an MCR501 rheometer (Anton Paar, Austria) equipped with a stainless steel truncated cone and plate geometry with R = 25 mm, $\alpha = 4^{o}$ and a = 0.053 mm, implemented with a Peltier element which provides temperature control (± 0.01 °C). Prior to testing, each sample was left to equilibrate at room temperature for 1 h. After that, it was loaded on the rheometer and the cone was lowered to 0.1 mm where it underwent an oscillatory pre-shearing (20% oscillatory strain, 80 $\frac{\text{rad}}{\text{s}}$ angular frequency) for 1 min. When the pre-shearing process ended, the cone was lowered slowly to 0.063 mm and the excess sample was trimmed. Finally, the cone was lowered to 0.053 mm (gap distance) and the sample was confined with PDMS oil in order to minimize water evaporation. The following protocol was applied to all six blends:

i) Dynamic strain sweep (DSS) at ω = 10 $\frac{\text{rad}}{\text{s}}$, from γ = 0.1% until a critical strain sufficiently large to probe the extend of linear response but such that the sample would not be expelled from the test geometry
ii) Dynamic frequency sweep (DFS) at γ = 1% and ω ranging from 100 to 0.01 $\frac{\text{rad}}{\text{s}}$
iii) Repeat DFS at γ = 1% and ω ranging from 0.1 to 100 $\frac{\text{rad}}{\text{s}}$
iv) Dynamic time sweep (DTS) at ω = 10 $\frac{\text{rad}}{\text{s}}$ with three segments:
    a) γ = 1% for about 60 seconds
    b) γ increasing to 200% in 4 seconds
    c) γ = 1% for 10 minutes
v) Rest for 30 minutes
vi) DFS at γ = 1% and ω ranging from 0.1 to 100 $\frac{\text{rad}}{\text{s}}$
vii) Transient shear rate test for shear rates 0.01, 0.02, 0.03, 0.05, 0.1, 0.2, 0.3, 0.5, 1, 2, 3 and 5 s^{-1} with rest time of 1.5 hours before the application of a new shear rate

The DSS test was conducted to determine the linear viscoelastic regime (LVE) [66]. Next, the first DFS test was executed in order to let the material reach a stable condition and the second in order to check possible change of the material over time. The three-step DTS test was designed in order to simulate the printing conditions of the material: a) pre-print, b) during printing, c) post-print. Viscosity is defined as the ratio of shear stress to shear rate and the difference in the material's viscosity pre-print and post-print is a metric of the recovery of the material and calculated using the formula: $\text{Recovery } \% = \frac{\text{Viscosity}_{\text{post-print}}}{\text{Viscosity}_{pre-print}} \times 100$ [67]. The recovery was measured using the post-print viscosity at 10 seconds after the end of step b). Subsequently, a DFS test was conducted to confirm that the material has reached the same LVE condition as in ii) above, and finally,

the transient shear test was performed in order to measure the viscosity of the material for a given shear rate after it reached steady state.

2.4. 3D Printing process

2.4.1. Design

The design of the multi-layered construct was made using the software provided by www.tinkercad.com. The 3D object was saved in a stl file which was sliced using Slic3r and a gcode file was produced that can be read by the printer. The construct has some intersected lines which hindered the multi-layered result. With some modifications in the gcode the

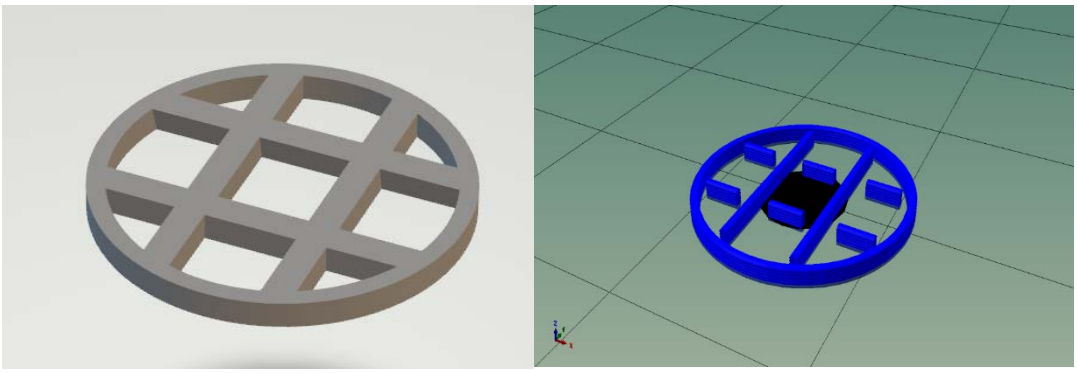

Figure 6. The 3D object as designed with the tinkercad software (left), the sliced and modified g-code model (middle), the 4% nHA result (right).

final design was made, which was used for all experiments mentioned below.

2.4.2. Parameter optimization

The parameters that affect the 3D printing process are the temperature of the cartridge, the inner diameter of the nozzle, the printing speed, the printing pressure, for a single layer and the distance between each layer (layer gap) for a multi-layer construct. The 0% nHA blend was studied for the parameter optimization. A single zig zag line (20 × 20 mm^2) was the object of optimization for a single layered construct. For a multi-layered construct the 3D design, that was mentioned above was used. Table 3 shows the values that were tested. Temperature was kept constant at 37 ^oC in order to improve cell viability and printing pressure was optimized specifically for each composition.

Table 3. Parameters tested for optimization

Inner Diameter (G)	Inner Diameter (mm)	Printing Speed (mm/s)	Layer Gap (mm)
25	0.25	2.5	0.10
22	0.41	5	0.15
		10	0.20

		20	0.25

i) Printing Speed: The optimal speed is one that has a high accuracy output while maintaining the corners of the line at 90°. Speeds of 2.5 to 10 mm/s resulted in over-extrusion, meaning that the width of the line was excessive and the speed of 25 mm/s resulted in the corners of the line to bent. At 20 mm/s, the printed line had high accuracy and the corners were not bent.

ii) Inner Diameter: Ideally in an extrusion-based 3D printer, the lower the inner diameter of the nozzle, the higher the accuracy of the 3D printed construct, therefore it a lower diameter is preferred to produce a highly detailed model. Even though, the nozzle with inner diameter of 0.25 mm showed excellent results in both single- and multi-layered constructs, the printing in a 24 well-plate always stopped because the nozzle clogged. This happened because there is temperature loss in the nozzle and the flow rate of the material was low and thus gelatin started to crosslink as the material inside the nozzle reached room temperature. Because of this, we worked with the 22G nozzle.

iii) Layer Gap: At the optimal layer gap the nozzle maintains a relatively low distance from the surface of each printed layer. At gaps lower than the optimal, the nozzle eventually prints below the current height of the construct (inside the construct) and at gaps higher than the optimal, the new printed layer makes little or no contact with the previous one. Based on these, we found that the optimal layer gap was 0.20 mm.

Table 4. Optimized printing parameters

Temperature (°C)	Inner Diameter (mm)	Printing Speed (mm/s)	Layer Gap (mm)
37	0.41	20	0.2

2.4.3. Printing

The hydrogel was loaded in a 10 ml syringe which was connected with a 3 ml cartridge via a female/female luer lock adapter (Cellink, Sweden). The cartridge was fixed with a 22G conical nozzle (Cellink, Sweden) and placed in the Inkredible+ bioprinter (Cellink, Sweden) and left to heat to 37 °C. The constructs were printed in a 24-well Corning® plate at room temperature, with 6 layers and at optimized printing conditions. Immediately after finishing a print in a well, the crosslinker was casted 1% $CaCl_2$ + 0.025% GTA for 15 min. Then, the constructs were thoroughly washed with ultrapure water and stored in 1x phosphate-buffered saline (PBS).

Figure 7. The Inkredible+ bioprinter

2.5. Filament diameter

To measure filament diameter, a single zig zag layer (20 × 20 mm^2) of each blend was printed with the same weight (0.02 g) in order to see the effect of the increasing concentration of nHa in the filament formation. Images from 9 different locations were taken using a microscope (Leica DM IRE2, Leica Microsystems) and analysed through ImageJ. The average diameter was calculated and divided by the inner diameter of the

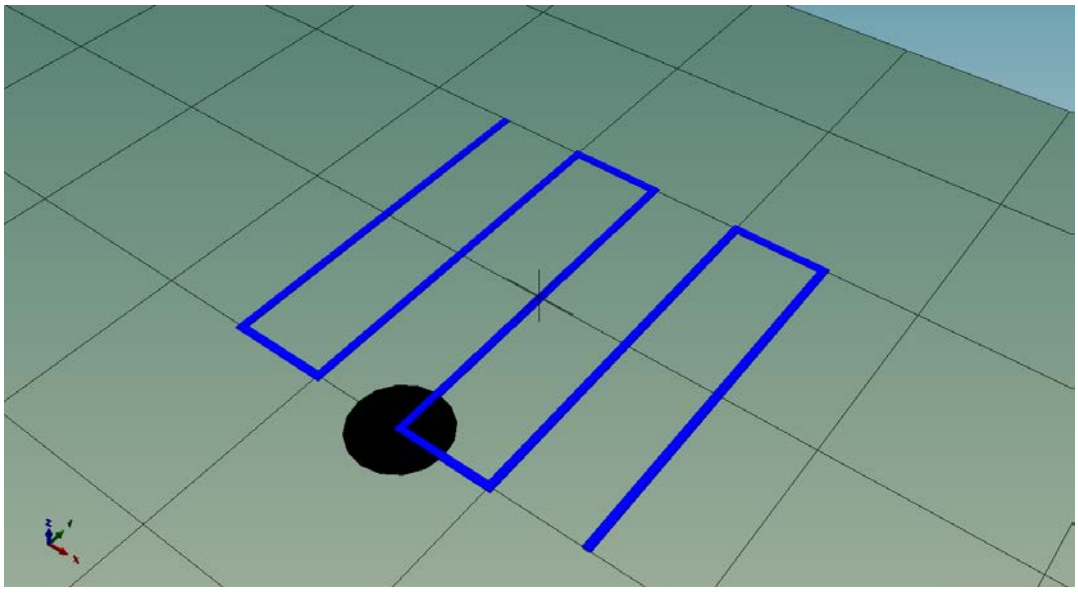

Figure 8. The g-code filament model

nozzle to find the filament accuracy.

2.6. Water content

The ability to uptake water is crucial for any potential tissue engineering construct as it correlates to the ability to uptake cell media and therefore it impacts greatly the cell viability and proliferation. To measure the water content of the hydrogels, n=3 constructs were printed as described above and their weight was measured at 0, 1, 3, 6, 24, 48 hours (wet weight). After the measurement they were freeze-dried for 24 hours and measured again (dry weight). The water content was calculated using the formula:

$$\text{Water } \% = \frac{\text{wet weight} - \text{dry weight}}{\text{dry weight}} \times 100$$

2.7. Optimal blend

An optimal blend was chosen based on the rheological measurements, the strand accuracy and the water content of the hydrogels to be further studied with the integration of cells inside the 3-D matrix.

2.8. Bioprinting

2.8.1. Cell culture

MC3T3-E1 pre-osteoblastic cells (DSMZ Braunschweig, Germany, ACC-210) were isolated from new-born mouse calvaria [68]. These cells have the capacity to differentiate into osteoblasts in vitro, so they are used as a model system for the investigation of cell adhesion, viability, proliferation and differentiation on biomaterials. MC3T3-E1 cells were cultured in α-modified minimum essential medium (a-MEM) (PAN-Biotech, Germany) supplemented with 10% (v/v) fetal bovine serum (FBS) (PAN-Biotech, Germany), 100 μg/ml penicillin and streptomycin (PAN-Biotech, Germany), 2 mM L-glutamine (PAN-Biotech, Germany) and 2.5 μg/ml Amphotericin (Gibco, Thermo Fisher Scientific, UK) in humidified incubator at 37^{o}C, 5% CO2. The culture medium was replaced twice weekly. The cells were detached using trypsin ethylenediaminetetraacetic acid (EDTA) (Gibco, Thermo Fisher Scientific, UK).

2.8.2. Bioprinting process

For the bioprinting experiments, at least 90% confluent MC3T3-E1 cell culture well plates were used at passage 16 to 18. The culture media was removed, the plates were washed with PBS 1x and cells were detached using 2.5% v/v Trypsin. The trypsin was neutralized by adding cell culture media and the cell suspension was loaded in a 15 ml falcon tube and centrifuged at 2400 rpm for 10 min. The supernatant was removed and then the cells were resuspended and counted in a hemocytometer in order to achieve a 1:10 cells to hydrogel ratio. Then, the cell suspension was loaded in a sterile 1 ml syringe and the hydrogel in a sterile 10 ml syringe after being exposed to UV for 30 min. The connection of the two syringes was achieved via a female/female luer lock adapter, the contents were mixed by going back and forth and finally the bioink was loaded to the 10 ml

syringe. The bioink had 3× 10^6 cells/ml cell concentration to hydrogel. Afterwards, a similar process was followed as described in paragraph 2.4.3. with the modification that the printer was moved into the biosafety cabinet to provide aseptic conditions and the bioprinted constructs were washed only with 1x PBS and with cell culture media. In the end, the cell-laden hydrogels were transferred to an incubator at 37 ^oC and 5% CO_2 until further use.

2.9. Evaluation of cell viability

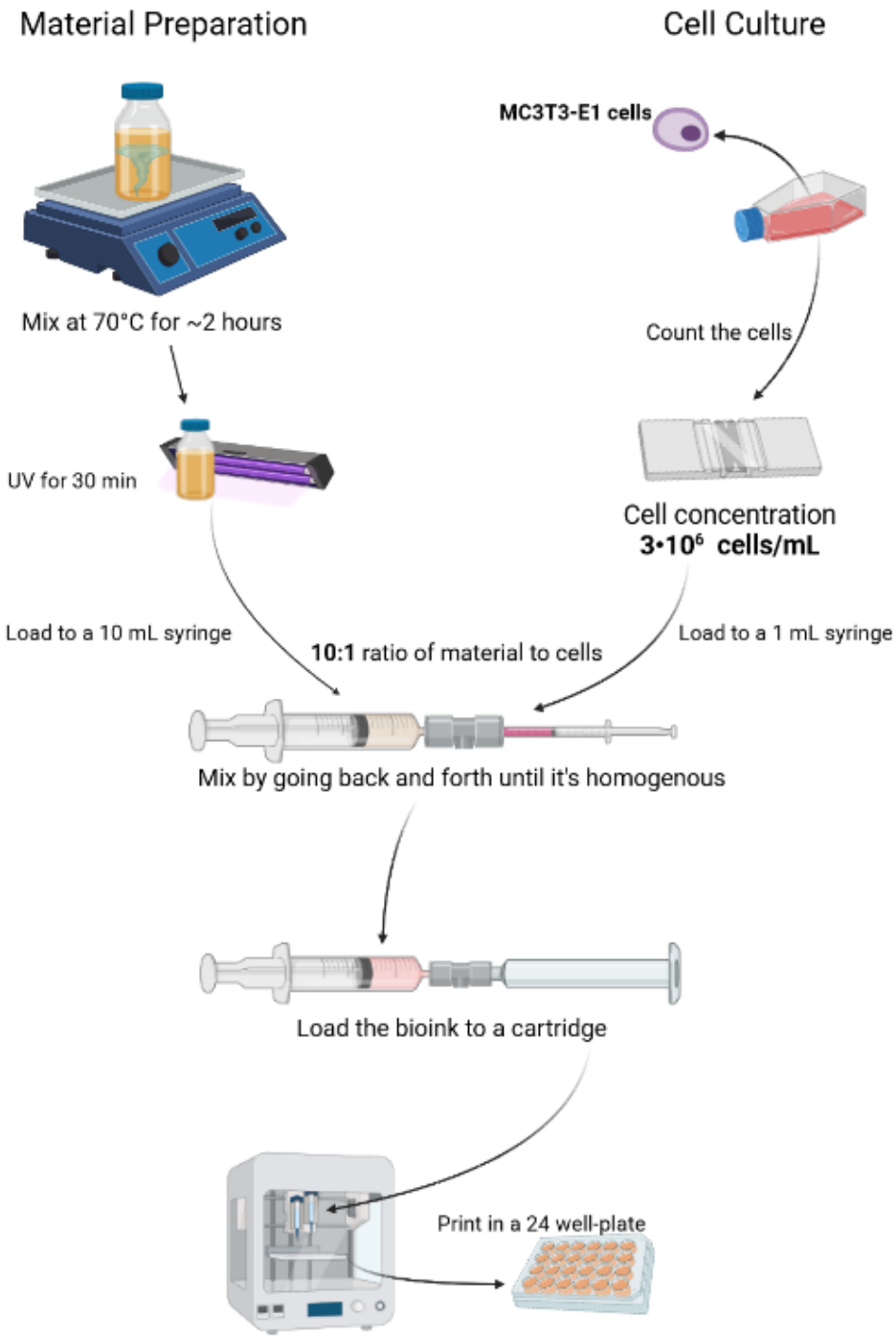

Figure 9 Graphical representation of the bioprinting process

2.9.1. Cell staining

Cell viability was assessed using a Live/Dead assay kit (Biotium, USA) following the protocol as described by the manufacturer. Briefly, the bioprinted constructs after 1, 4 and 8 days of culture were washed twice with PBS and then incubated in a working solution with 2 µM calcein-AM (494 nm excitation, 517 nm emission) and 4 µM ethidium homodimer III (EthD-III) (532 nm excitation, 625 nm emission) at room temperature for 30 min. Then, they were washed again with PBS, stored in culture medium and imaged using a high content analysis system (Operetta CLS, Perkin Elmer). Cells were characterized as live when they fluoresced from calcein-AM (green channel) and dead when they fluoresced from either solely from EthD-III (red channel) or from both stains. Cells were quantified using dedicated image analysis software (Harmony 4.1, PerkinElmer).

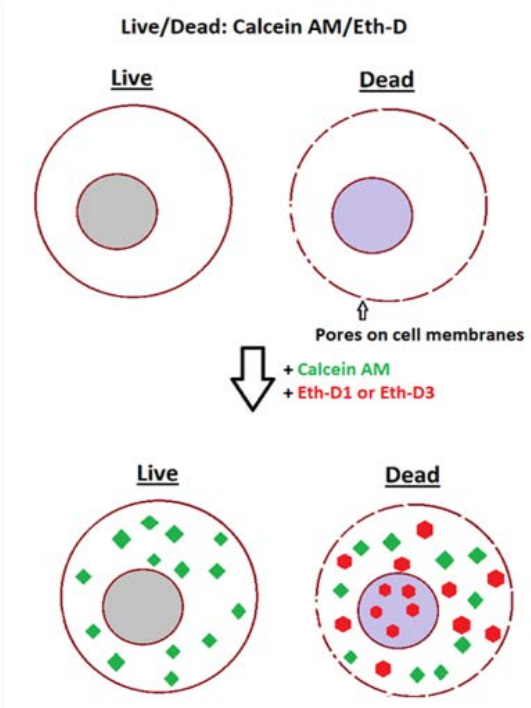

Figure 10. Live/Dead staining adapted from [5]

2.9.2. High content analysis system

Light from a 300 W xenon lamp with a continuous spectrum of 350-680 nm is emitted, passes through an excitation filter wheel and is guided via two mirrors which are mounted on a slider. The emitted light travels through an objective lens and excites the sample. A transmission light source is situated above the sample for brightfield imaging, either separately or combined with fluorescence imaging. Fluorescence emission and transmitted light signals are filtered by an emission filter wheel and collected through a high sensitivity Peltier cooled CCD camera [69].

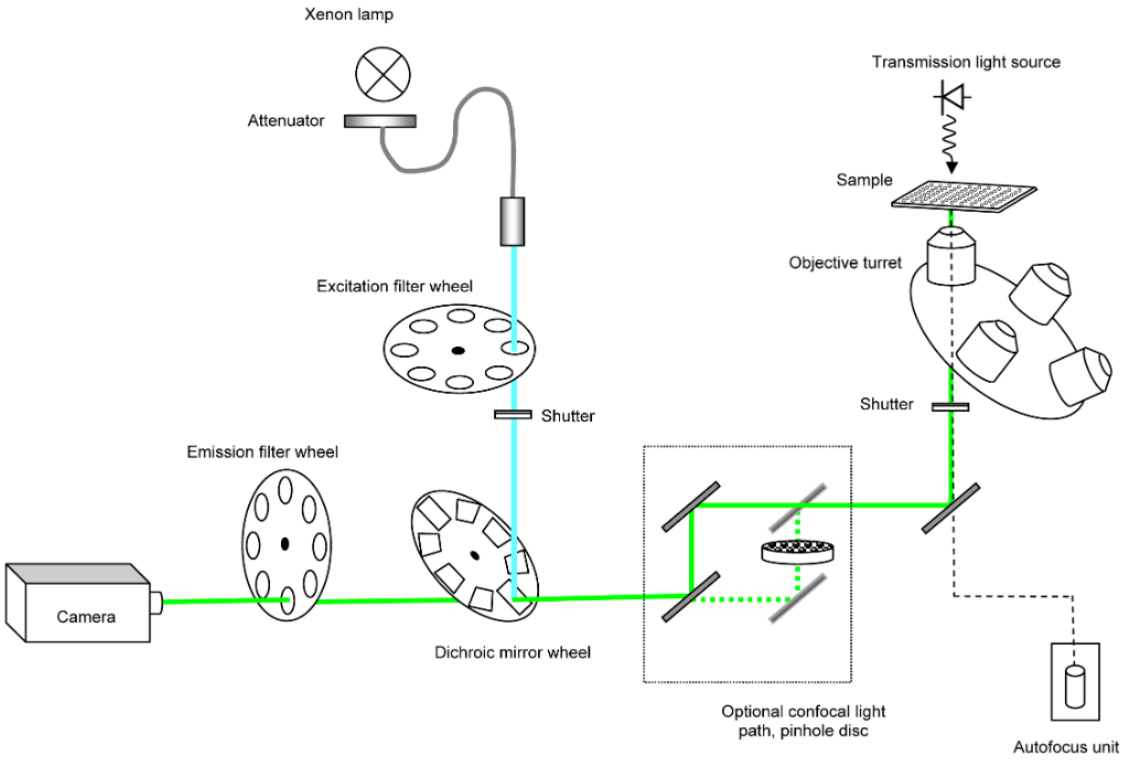

Figure 11. Graphical representation of high content analysis configuration

2.9.3. Cell imaging and quantification

Imaging of the samples was performed using a 50 µm step (z-axis) and adjusted to incorporate the whole height of the construct. Total cell number was estimated in individual z-axis stacks. Cells that had the same x, y coordinates or coordinates that differ in one pixel in neighbouring stacks, were merged to correct for photon's refraction. This took place in excel using a PIVOT table and subsequently using an in-house algorithm in Python.

2.10. Statistical analysis

Statistical analysis was performed for the filament accuracy and water content using the one-way and two-way ANOVA multiple comparison test in GraphPad Prism software (GraphPad 8.0, San Diego, CA, USA). A *p*-value of < 0.05 was considered significant.

3. Results

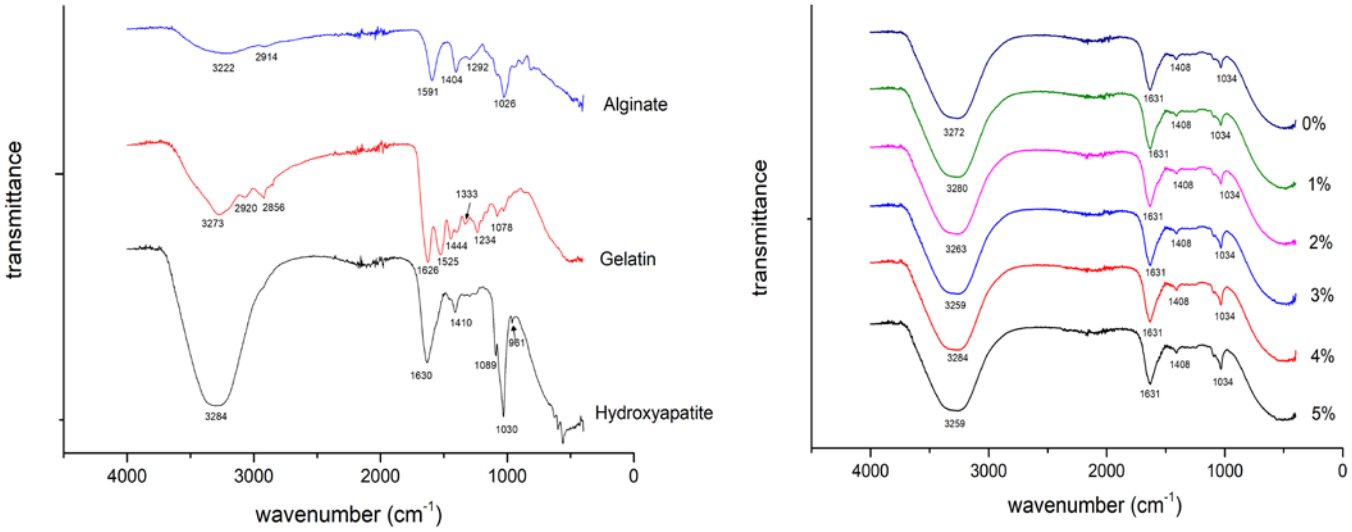

Figure 12. FTIR spectra of pure materials (left) and hydrogel blends (right)

3.1. FTIR

The FTIR transmittance spectra of the pure materials and all six blends and their peaks are shown in Figure 11. Alginate's vibration bands of the CO_2^- were located at 1591 cm^{-1} (antisymmetric stretch) and at 1412 cm^{-1} (symmetric stretch). The wide band around 3222 cm^{-1} is due to stretch of OH and the peak at 2914 cm^{-1} is caused by CH stretching. At 1297 cm^{-1} a skeletal vibration occurs followed by the antisymmetric stretch of C – O – C at 1026 cm^{-1}. The spectra of alginate are in agreement with results from Lawrie et al. [70] Gelatin bands from bovine skin were described by Ibrahim et al. [71]. The characteristic peaks of amide groups were located: around 3273 cm^{-1} due to NH stretching, at 1626 cm^{-1} due to C=O and CN stretching (amide I), at 1525 cm^{-1} (amide II) and at 1234 cm^{-1} (amide III). The vibration of CH_2 is represented by four bands: at 2920 cm^{-1} (antisymmetric stretch), at 2856 cm^{-1} (symmetric stretch), at 1444 cm^{-1} (bending) and at 1333 cm^{-1} (wagging). The band at 1078 cm^{-1} corresponds to the CH_3 amide group. Hydroxyapatite showed three characteristic peaks at 961, 1030 and 1089 cm^{-1}, which indicate the presence of phosphate ion (PO_4^{3-}) groups. The peak at 1630 and the broad band at 3000-3700 cm^{-1} are attributed to the bands of lattice water. The peak at 1410 cm^{-1} is a result from CO_2^- adsorption by the apatite [72]. All six blends displayed the same bands: a broad band around 3000-3700 cm^{-1} mainly due to water, a peak at 1631 cm^{-1} that is a result from the convergence of water, CO_2^- (antisymmetric) and amide I stretching, a small peak at 1408 cm^{-1} due to CO_2^- (symmetric) stretch and a peak at 1034 cm^{-1} due to phosphate ion groups.

3.2. Filament diameter

The filament diameters and the filament accuracy for the increasing concentration of nHa are shown in Figure 12. It can be seen that the augmentation of nHa results in thinner filaments and higher filament accuracy. There is a significant increase ($p<0.05$) as the percentage of nHA rises while above 3% nHA there is no statistical difference in filament accuracy. Table 5 summarizes the data shown in Figure 12 with the addition of the printing

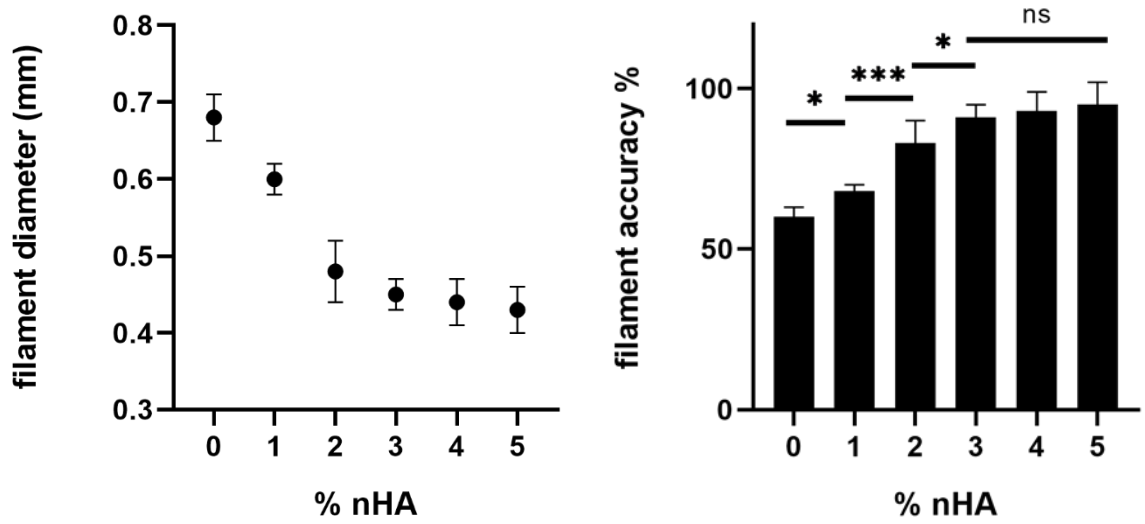

Figure 13. Filament diameter (left) and filament accuracy (right) vs % of nHA

pressure for each blend that resulted in 0.02 g of extruded filament.

Table 5. Printing pressures and filament diameters for 0.02 g of filament

Percentage of nHA (%)	Printing pressure (kPa)	Filament diameter (mm)	Filament accuracy (%)
0	180	0.68 ± 0.03	60 ± 3
1	218	0.60 ± 0.02	68 ± 2
2	228	0.48 ± 0.04	83 ± 7
3	250	0.45 ± 0.02	91 ± 4
4	260	0.44 ± 0.03	93 ± 6
5	275	0.43 ± 0.03	95 ± 7

3.3. Rheology

The DFS test showed that with the increment of the concentration of nHA resulted in higher G' values and reduced the loss tangent (tanδ), with the 4% and 5% nHA concentrations behaving almost the same. From the steady states of the transient shear rate tests, a flow curve was created and a power model was utilized to fit the results. The power-law model $\boldsymbol{\eta = K\dot{\gamma}^{n-1}}$ has been used where η represents viscosity, γ̇ denotes the shear rate, n is the power-law index and K is the consistency index. Finally, the recovery was

measured from the three-step DTS, for all blends. The 0% nHA blend exhibited the highest recovery after 10 seconds at 89% ± 2% and the lowest was from blend 4 at 73% ± 3%. Table

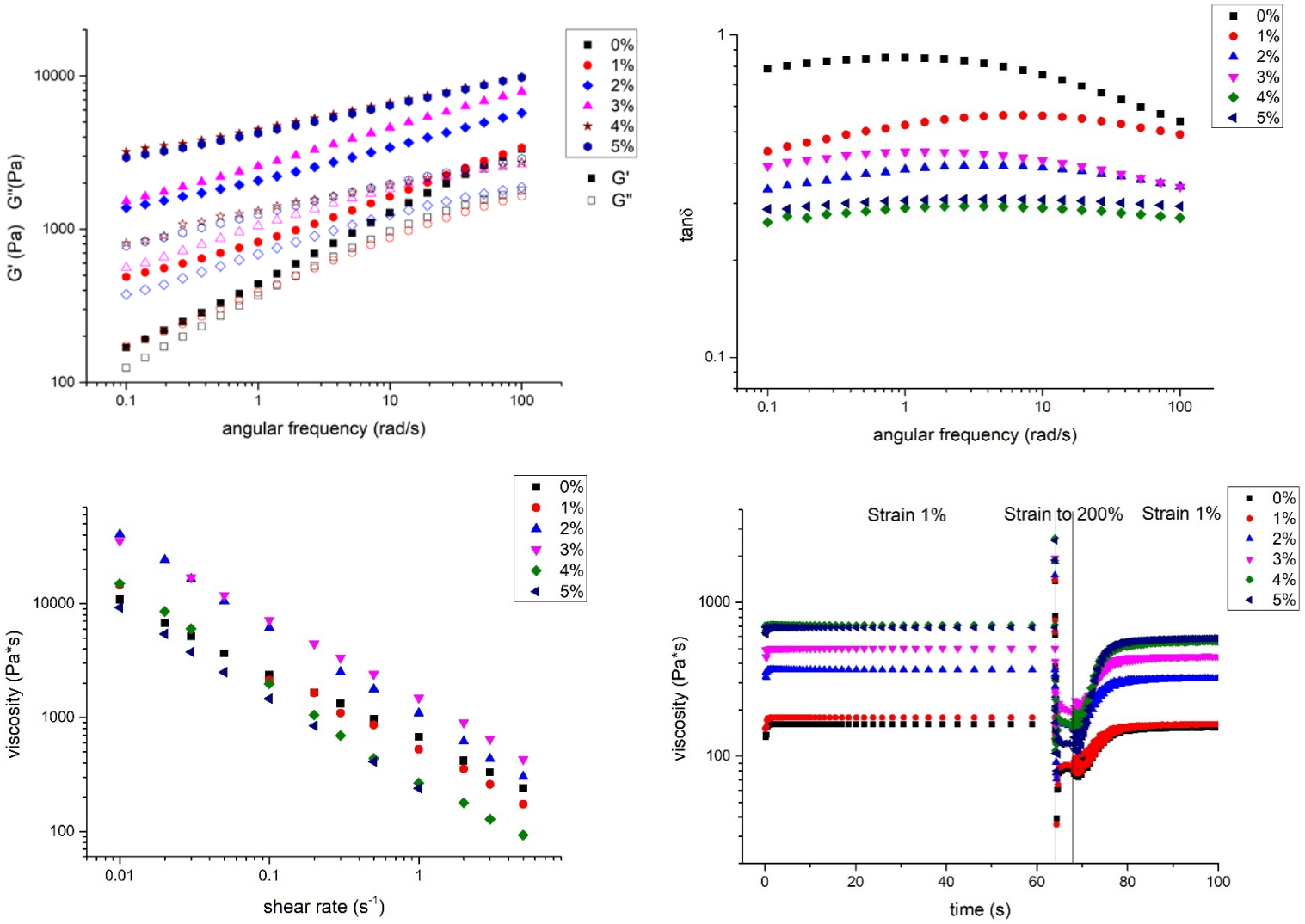

Figure 14. Rheological evaluation of all blends. Storage modulus G' and loss modulus G'' vs angular frequency (upper left), loss tangent vs angular frequency (upper right), flow curve (lower left), recover testing (lower right)

6 shows the power-law exponents and the recoveries of the blends.

Table 6. Power law exponents and recovery at 10 seconds

Percentage of nHA (%)	Power law exponents	Recovery at 10 seconds (%)
0	-0.600 ± 0.006	89 ± 2
1	-0.69 ± 0.02	84 ± 3
2	-0.788 ± 0.007	82 ± 3
3	-0.704 ± 0.005	83 ± 3
4	-0.84 ± 0.02	73 ± 3

5	-0.794 ± 0.004	78 ± 2

3.4. Water content

Water content analysis showed that all blends exhibited very significant increase ($p < 0.0001$) in water content between 0 and 1 h and they reached equilibrium state after 6 h as there were no significant differences between 6 and 24 h in all blends.

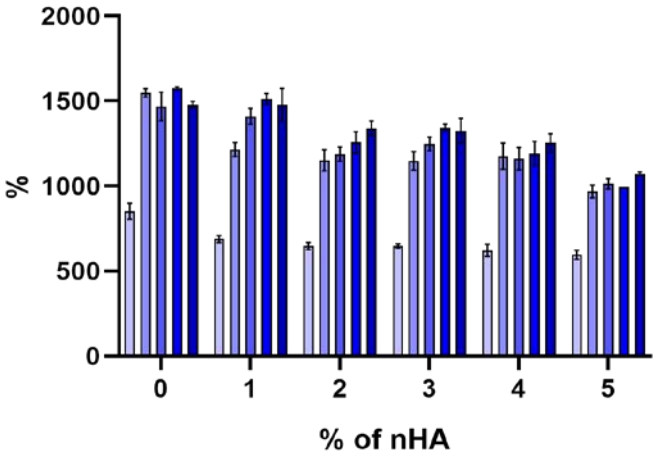

Figure 15. Water content of blends measured in various time points

Table 7. Water content at equilibrium

Percentage of nHA (%)	Water content at equilibrium (%)
0	1575 ± 9
1	1510 ± 30
2	1260 ± 60
3	1340 ± 20
4	1190 ± 70
5	994 ± 3

3.5. Optimal blend

Taking into consideration the printing accuracy, the recovery and the water content percentage, the 7% Alg – 8% Gel – 3% nHA was chosen as the optimal blend for it had a high accuracy (>90%), high recovery (>80%) and water content was 1340 ± 20 after 6 h.

3.6. Cell viability

Cell viability analysis showed that at Day 1 cells had very low viability (less than 10%) and at Day 8 had 21% ± 6% viability.

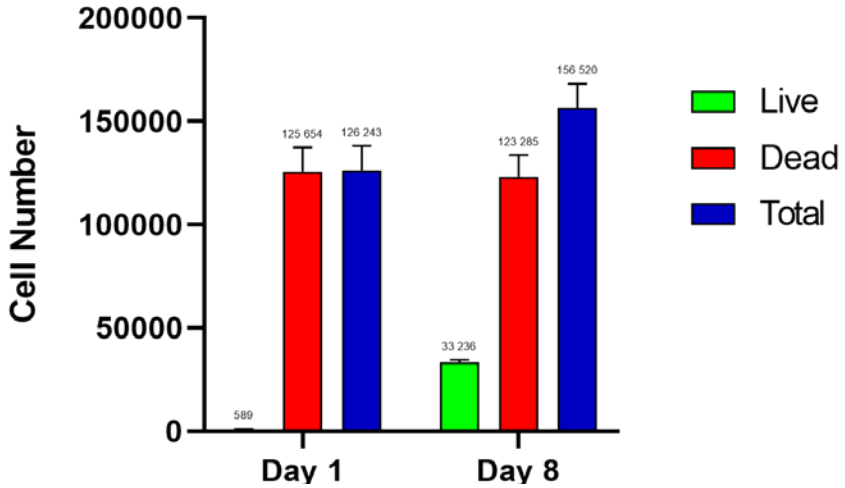

Figure 16. Cell viability quantification

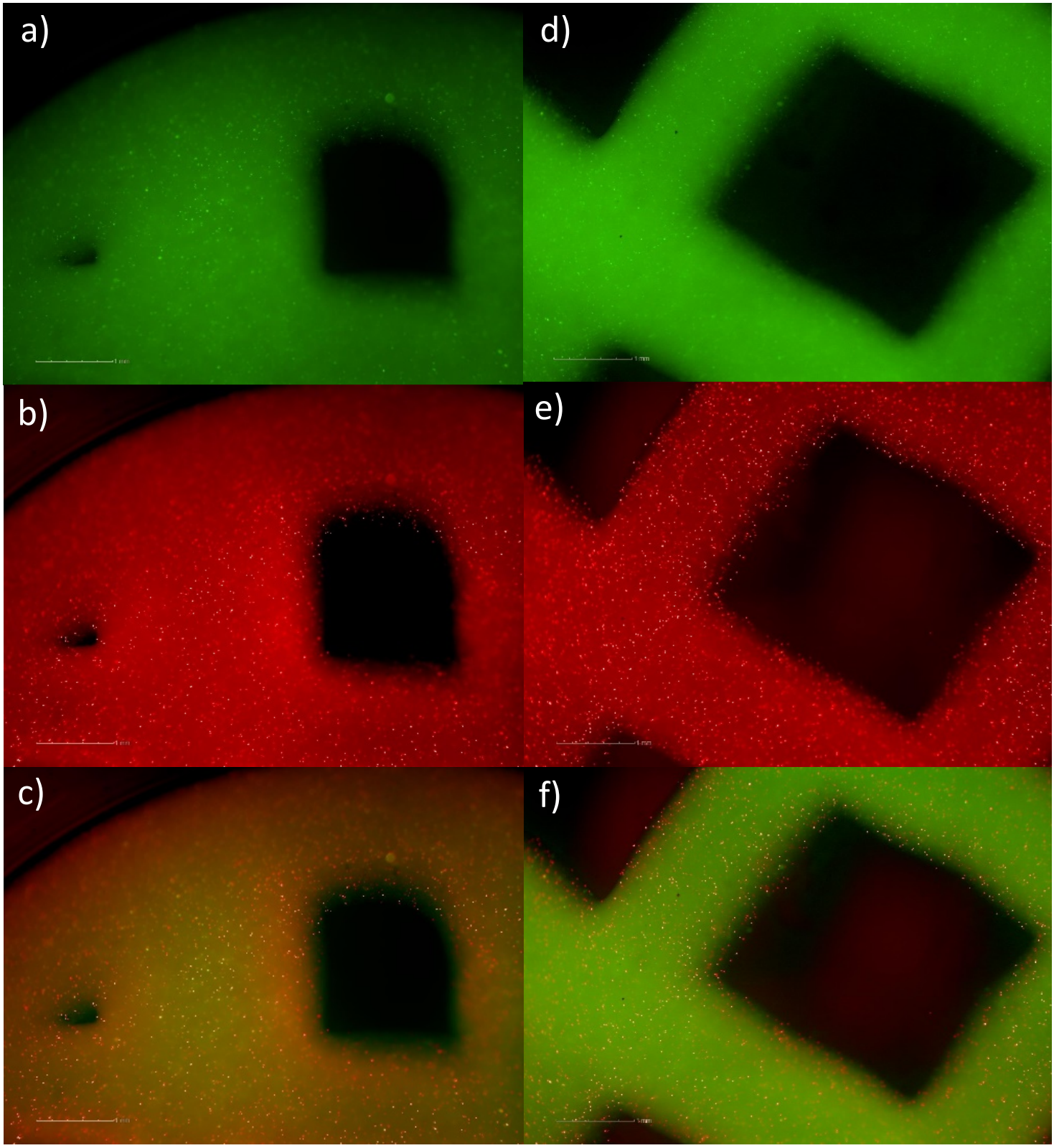

Figure 17. Cell viability imaging at Day 1(a)-c)) and at Day 8 (d)-f)). a) and d) show calcein-AM staining, b) and e) show EthD-III staining and c) and f) is the merged result.

4. Discussion

Bioprinted alginate - gelatin blends have been thoroughly studied for tissue engineering applications. It has been demonstrated that mouse embryonic stem cells maintained 90% viability after printing and their pluripotency after 7 days in culture [73]. The same group also investigated the rheological characteristics of alginate – gelatin hydrogels while proving a correlation between cell viability and holding printing time [74]. Another group reported the *in vitro* formation of tumor co-culture spheroids within the hydrogel and the crosstalk between co-cultured cells [75]. When bioactive glass was added to an alginate – gelatin bioink, Saos-2 cells (osteosarcoma) died immediately after printing but human bone marrow-derived mesenchymal stem cells survived the printing process and maintained good viability for 14 days. The study suggests that the viscosity of the bioink influences the short- and long-term viability of cells and that the bioink should be tailored to suit the cell type [49]. An overlay of agarose and calcium salt of polyphosphate induced the capacity of Saos-2 cells, within an alginate-gelatin scaffold, to proliferate and when cultured for 7 days in an osteogenic cocktail, the cells reacted strongly with Alizarin Red S suggesting high calcium mineralization [76]. Therefore, Alg – Gel blends exhibit high impact in tissue engineering applications by the means of bioprinting and especially in bone tissue engineering, thus proving their versatility as a material-candidate in these applications.

In this study, the characterization of the hydrogel blends through the means of FTIR displayed an increasing peak of phosphate ion groups at 1034 cm^{-1} as the nHA concentration increased.

The ability of an ink to extrude as a consistent filament, the formation of the first layer, flow behaviour and crosslinking capabilities are all properties which significantly impact ink printability [77, 78]. It is expected that lower viscosity gels would pool more due to a less dense network which is evidenced by the lower concentrations exhibiting wider strands [79]. The doping of nHA in the Alg – Gel matrix, increased the viscosity of the bioink and therefore it is expected that bioinks with high HA concentration are able to produce more accurate strands than those of low concentrations as reported here.

The loss tangent carries information on the ratio between the viscous and the elastic portion of the viscoelastic deformation behavior [80]. In this study, the augmentation of the nHA percentage reduced the loss tangent of the bioink which is in accordance with studies that report that the addition of HA aggravates the solid-like behaviour of the ink and it renders it more viscous [81, 82]. A rheological study on Alg – Gel bioinks focused on printability concluded that when tan(δ) was approximately between 0.25 and 0.45 the Alg – Gel bioinks were printed with relatively good smoothness without compromising structural integrity [83]. This is in agreement with the results from the filament diameter and accuracy testing as the inks above 2% nHA exhibited over 90% filament accuracy and their tan(δ) ranged from 0.26 to 0.43.

Fluids showing a linear relationship between shear stress and shear rate are termed Newtonian (n = 1) and fluids that deviate from the linearity are defined non-Newtonian (n ≠ 1) [84]. Time-independent non-Newtonian fluids are usually classified as shear thinning (n < 1), where the viscosity decreases as shear rate increases and shear thickening (n > 1), where viscosity increases as shear rate increases [66]. All blends exhibited shear thinning behaviour, which is a desired characteristic in extrusion printing [85].

A condition that is beneficial in order to produce high shape fidelity prints is the rapid recovery of the bioink from the applied shear stresses [86]. The doping of Alg – Gel hydrogels with nHA decreased the recovery of the bioink which is in agreement with a recent study [81]. This is possibly due to the fact that HA as a ceramic imparts brittleness in the bioink, where the stress, after a point, can generate permanent (irreversible) deformation (i.e. plastic deformation) [8].

Hydrogels are able to absorb large quantities of water or biological fluids and thus have the potential to be used as matrices for cells in tissue engineering [87]. In the present study, the addition of nHA in the Alg – Gel matrix resulted in a decrease of water content as the percentage of nHA increased, a trend confirmed by various studies [63, 88, 89]. Nevertheless, the degree of water content in all blends was sufficient and considering the cell proliferation of this study, the diffusion of nutrients throughout the hydrogel was sufficient.

MC3T3-E1 pre-osteoblastic cells, exhibit, when good attachment occurs, a spindle-like elongated shape [90]. The images in this study, show that the cells have a round-like (spherical) morphology which could be attributed to the fact that the hydrogel possesses high polymer concentration (15% w/v in total) and therefore the cells do not have the necessary space in order to elongate. Hence, the cells seem to be very constricted within the hydrogel matrix and it is probable that they experience high mechanical stresses. Combined with the stresses induced in the mixing of the material with the cells and the fact that the chemical crosslinking that was used is cytotoxic, a low cell viability is expected in early time points.

Calcein-AM is a membrane-permeant, non-fluorescent esterase substrate, which enters the cytoplasm and is cleaved by esterases in live cells to yield the green fluorescent dye calcein. It is negatively charged and cell membrane-impermeant, and consequently is retained in the cytoplasm of viable cells. Dead cells do not stain with calcein due to lack of esterase activity. EthD-III is a plasma membrane-impermeant DNA dye that is excluded by viable cells. EthD-III is virtually non-fluorescent until it binds DNA and also, it penetrated cells with compromised plasma membranes and stains the nucleus with bright red fluorescence. Usually, cells are stained with either one stain denoting them as either living, when stained with calcein-AM or dead, when stained with EthD-III. In this study, some cells were stained with both dyes. This is possibly due to the fact that when cells are in the early stage of apoptosis (programmed cell death) calcein can be present in the cell and as the

plasma membrane deteriorates (a feature of late apoptosis) EthD-III can enter into the cell while calcein is still trapped. Therefore, it is possible that cells can be stained with both dyes.

Cell viability analysis showed that even though the viability at Day 1 was very low, at Day 8 it was significantly higher ($p<0.0001$), therefore cells proliferated inside the composite's matrix. Measuring cell viability at later time points (i.e. Day 15, Day 30) could illuminate cells' behavior encapsulated in the composite's matrix.

5. Conclusion

Examination of the addition of nHA in an Alg – Gel hydrogel in this study shows that the nHA particles affect the printing, rheological and mechanical behavior of the final construct. Augmentation of HA reduced the diameter of the extruded filament and the loss tangent implying that it provides a solid-like behavior while it lowered the recovery as it possesses brittle nature. The water concentration within the matrix was also reduced by the addition of HA as the matrix was more condense. Finally, cells had low viability at early time points but exhibited signs of proliferation.

6. Future studies

Since cells proliferated inside the construct's matrix, an investigation of long-term viability could clarify their behavior with the composite's matrix. Also, an examination of the mechanical response of the material by compression testing and its change caused by the encapsulation of cells would be of a great scientific interest as it would show how the cells affect the mechanical properties in various time points. It has been reported that matrix stress relaxation can regulate cell proliferation and promote bone regeneration [91]. Thus, mechanical stimulation by compression, using a bioreactor, could possibly confirm these findings while it could potentially induce cell differentiation and improve the mechanical properties of the construct.

7. References

1. Lee, K.Y. and D.J. Mooney, *Alginate: Properties and biomedical applications.* Progress in Polymer Science, 2012. **37**(1): p. 106-126.
2. Braccini, I. and S. Pérez, *Molecular Basis of Ca2+-Induced Gelation in Alginates and Pectins: The Egg-Box Model Revisited.* Biomacromolecules, 2001. **2**(4): p. 1089-1096.
3. Lanza, R., et al., *Principles of tissue engineering*. 2020: Academic press.
4. Kommareddy, S., D.B. Shenoy, and M.M. Amiji, *Gelatin Nanoparticles and Their Biofunctionalization*, in *Nanotechnologies for the Life Sciences*. 2007.
5. Nguyen, P.A.H., et al., *How to select the appropriate method(s) of cytotoxicity analysis of mammalian cells at biointerfaces: A tutorial.* Biointerphases, 2020. **15**(3): p. 031201.
6. Ibrahim, M., et al., *Hydroxyapatite, a multifunctional material for air, water and soil pollution control: A review.* Journal of Hazardous Materials, 2020. **383**: p. 121139.
7. Grainger, D., *The Williams dictionary of biomaterials.* Materials Today, 1999. **3**(2): p. 29.
8. Wagner, W.R., et al., *Biomaterials science: An introduction to materials in medicine*. 2020: Academic Press.
9. Temenoff, J.S. and A.G. Mikos, *Biomaterials: the intersection of biology and materials science*. Vol. 1. 2008: Pearson/Prentice Hall Upper Saddle River, NJ, USA:.
10. Wong, J.Y. and J.D. Bronzino, *Biomaterials*. 2007, Taylor & Francis group, Boca Raton, London, New York.
11. Persidis, A., *Tissue engineering.* Nature Biotechnology, 1999. **17**(5): p. 508-510.
12. Atala, A. and D.J. Mooney, *Synthetic biodegradable polymer scaffolds*. 1997: Springer Science & Business Media.
13. Atala, A. and J.J. Yoo, *Essentials of 3D biofabrication and translation*. 2015: Academic Press.
14. Khademhosseini, A. and G. Camci-Unal, *3D Bioprinting in Regenerative Engineering: Principles and Applications*. 2018: CRC Press.
15. Boularaoui, S., et al., *An overview of extrusion-based bioprinting with a focus on induced shear stress and its effect on cell viability.* Bioprinting, 2020. **20**: p. e00093.
16. Harley, W.S., et al., *Advances in biofabrication techniques towards functional bioprinted heterogeneous engineered tissues: A comprehensive review.* Bioprinting, 2021. **23**: p. e00147.
17. Li, X., et al., *Inkjet Bioprinting of Biomaterials.* Chemical Reviews, 2020. **120**(19): p. 10793-10833.
18. Liang, R., et al., *Lithography-Based 3D Bioprinting and Bioinks for Bone Repair and Regeneration.* ACS Biomaterials Science & Engineering, 2021. **7**(3): p. 806-816.
19. Antoshin, A.A., et al., *LIFT-bioprinting, is it worth it?* Bioprinting, 2019. **15**: p. e00052.
20. Bilezikian, J.P., et al., *Principles of bone biology.* 2019.
21. Wang, X., et al., *Fundamental biomechanics in bone tissue engineering.* Synthesis Lectures on Tissue Engineering, 2010. **2**(1): p. 1-225.
22. Hollinger, J.O., et al., *Bone tissue engineering*. 2004: CRC press.
23. Pawelec, K. and J.A. Planell, *Bone repair biomaterials: Regeneration and clinical applications.* 2018.

24. Zhang, L.G., J.P. Fisher, and K. Leong, *3D bioprinting and nanotechnology in tissue engineering and regenerative medicine*. 2015: academic press.
25. Boccaccini, A.R. and P.X. Ma, *Tissue engineering using ceramics and polymers*. 2014: Elsevier.
26. Łabowska, M.B., I. Michalak, and J. Detyna, *Methods of extraction, physicochemical properties of alginates and their applications in biomedical field – a review.* Open Chemistry, 2019. **17**(1): p. 738-762.
27. Burdick, J.A. and R.L. Mauck, *Biomaterials for tissue engineering applications: a review of the past and future trends.* 2010.
28. Shilpa, A., S.S. Agrawal, and A.R. Ray, *Controlled Delivery of Drugs from Alginate Matrix.* Journal of Macromolecular Science, Part C, 2003. **43**(2): p. 187-221.
29. Gombotz, W.R. and S. Wee, *Protein release from alginate matrices.* Advanced Drug Delivery Reviews, 1998. **31**(3): p. 267-285.
30. Hasnain, M.S. and A.K. Nayak, *Natural Polysaccharides in Drug Delivery and Biomedical Applications*. 2019: Academic Press.
31. Augst, A.D., H.J. Kong, and D.J. Mooney, *Alginate Hydrogels as Biomaterials.* Macromolecular Bioscience, 2006. **6**(8): p. 623-633.
32. Kumar Giri, T., et al., *Alginate based hydrogel as a potential biopolymeric carrier for drug delivery and cell delivery systems: present status and applications.* Current drug delivery, 2012. **9**(6): p. 539-555.
33. Rastogi, P. and B. Kandasubramanian, *Review of alginate-based hydrogel bioprinting for application in tissue engineering.* Biofabrication, 2019. **11**(4): p. 042001.
34. Park, J., et al., *Three dimensional cell printing with sulfated alginate for improved bone morphogenetic protein-2 delivery and osteogenesis in bone tissue engineering.* Carbohydrate Polymers, 2018. **196**: p. 217-224.
35. Gu, Q., et al., *Functional 3D Neural Mini-Tissues from Printed Gel-Based Bioink and Human Neural Stem Cells.* Advanced Healthcare Materials, 2016. **5**(12): p. 1429-1438.
36. Isaacson, A., S. Swioklo, and C.J. Connon, *3D bioprinting of a corneal stroma equivalent.* Experimental Eye Research, 2018. **173**: p. 188-193.
37. Lee, J.-S., et al., *3D printing of composite tissue with complex shape applied to ear regeneration.* Biofabrication, 2014. **6**(2): p. 024103.
38. Datta, S., et al., *Alginate-honey bioinks with improved cell responses for applications as bioprinted tissue engineered constructs.* Journal of Materials Research, 2018. **33**(14): p. 2029-2039.
39. Athirasala, A., et al., *A dentin-derived hydrogel bioink for 3D bioprinting of cell laden scaffolds for regenerative dentistry.* Biofabrication, 2018. **10**(2): p. 024101.
40. Yang, X., et al., *Collagen-alginate as bioink for three-dimensional (3D) cell printing based cartilage tissue engineering.* Materials Science and Engineering: C, 2018. **83**: p. 195-201.
41. Izadifar, M., et al., *Bioprinting pattern-dependent electrical/mechanical behavior of cardiac alginate implants: characterization and ex vivo phase-contrast microtomography assessment.* Tissue Engineering Part C: Methods, 2017. **23**(9): p. 548-564.
42. Kang, K., et al., *Three-dimensional bioprinting of hepatic structures with directly converted hepatocyte-like cells.* Tissue Engineering Part A, 2018. **24**(7-8): p. 576-583.
43. Peppas, N.A., *Biomedical applications of hydrogels handbook*. 2010: Springer Science & Business Media.
44. Su, K. and C. Wang, *Recent advances in the use of gelatin in biomedical research.* Biotechnology Letters, 2015. **37**(11): p. 2139-2145.
45. Neves, N.M. and R.L. Reis, *Biomaterials from nature for advanced devices and therapies*. 2016: John Wiley & Sons.
46. Bigi, A., et al., *Mechanical and thermal properties of gelatin films at different degrees of glutaraldehyde crosslinking.* Biomaterials, 2001. **22**(8): p. 763-768.

47. Olde Damink, L.H.H., et al., *Glutaraldehyde as a crosslinking agent for collagen-based biomaterials.* Journal of Materials Science: Materials in Medicine, 1995. **6**(8): p. 460-472.
48. Bello, A.B., et al., *Engineering and functionalization of gelatin biomaterials: From cell culture to medical applications.* Tissue Engineering Part B: Reviews, 2020. **26**(2): p. 164-180.
49. Ojansivu, M., et al., *Wood-based nanocellulose and bioactive glass modified gelatin–alginate bioinks for 3D bioprinting of bone cells.* Biofabrication, 2019. **11**(3): p. 035010.
50. Joung, D., et al., *3D Printed Stem-Cell Derived Neural Progenitors Generate Spinal Cord Scaffolds.* Advanced Functional Materials, 2018. **28**(39): p. 1801850.
51. Somasekharan, L.T., et al., *Biofabrication of skin tissue constructs using alginate, gelatin and diethylaminoethyl cellulose bioink.* International Journal of Biological Macromolecules, 2021. **189**: p. 398-409.
52. Liu, P., et al., *3D bioprinting and in vitro study of bilayered membranous construct with human cells-laden alginate/gelatin composite hydrogels.* Colloids and Surfaces B: Biointerfaces, 2019. **181**: p. 1026-1034.
53. Singh, Y.P., A. Bandyopadhyay, and B.B. Mandal, *3D Bioprinting Using Cross-Linker-Free Silk–Gelatin Bioink for Cartilage Tissue Engineering.* ACS Applied Materials & Interfaces, 2019. **11**(37): p. 33684-33696.
54. Anil Kumar, S., et al., *A Visible Light-Cross-Linkable, Fibrin–Gelatin-Based Bioprinted Construct with Human Cardiomyocytes and Fibroblasts.* ACS Biomaterials Science & Engineering, 2019. **5**(9): p. 4551-4563.
55. Mahdavi, S.S., et al., *Stereolithography 3D Bioprinting Method for Fabrication of Human Corneal Stroma Equivalent.* Annals of biomedical engineering, 2020. **48**(7): p. 1955-1970.
56. Han, Y., et al., *Three-Dimensional Printing of Hydroxyapatite Composites for Biomedical Application.* Crystals, 2021. **11**(4): p. 353.
57. LeGeros, R.Z., *Properties of Osteoconductive Biomaterials: Calcium Phosphates.* Clinical Orthopaedics and Related Research®, 2002. **395**: p. 81-98.
58. LeGeros, R.Z., *Calcium Phosphate-Based Osteoinductive Materials.* Chemical Reviews, 2008. **108**(11): p. 4742-4753.
59. Liu, X., et al., *Cell responses to two kinds of nanohydroxyapatite with different sizes and crystallinities.* International journal of nanomedicine, 2012. **7**: p. 1239-1250.
60. Fan, Y., et al., *3D Composite Cell Printing Gelatin/Sodium Alginate/n-HAP Bioscaffold.* Journal of Physics: Conference Series, 2019. **1213**: p. 042020.
61. Bendtsen, S.T., S.P. Quinnell, and M. Wei, *Development of a novel alginate-polyvinyl alcohol-hydroxyapatite hydrogel for 3D bioprinting bone tissue engineered scaffolds.* Journal of Biomedical Materials Research Part A, 2017. **105**(5): p. 1457-1468.
62. Demirtaş, T.T., G. Irmak, and M. Gümüşderelioğlu, *A bioprintable form of chitosan hydrogel for bone tissue engineering.* Biofabrication, 2017. **9**(3): p. 035003.
63. Wenz, A., et al., *Bone matrix production in hydroxyapatite-modified hydrogels suitable for bone bioprinting.* Biofabrication, 2017. **9**(4): p. 044103.
64. Goudoulas, T.B. and N. Germann, *Phase transition kinetics and rheology of gelatin-alginate mixtures.* Food Hydrocolloids, 2017. **66**: p. 49-60.
65. Griffiths, P.R. and J.A. De Haseth, *Fourier transform infrared spectrometry*. Vol. 171. 2007: John Wiley & Sons.
66. Barnes, H.A., J.F. Hutton, and K. Walters, *An introduction to rheology*. Elsevier. Vol. 3. 1989.
67. Rastin, H., et al., *3D Bioprinting of Methylcellulose/Gelatin-Methacryloyl (MC/GelMA) Bioink with High Shape Integrity.* ACS Applied Bio Materials, 2020. **3**(3): p. 1815-1826.
68. Hadjicharalambous, C., et al., *Effect of Porosity of Alumina and Zirconia Ceramics toward Pre-Osteoblast Response.* Frontiers in Bioengineering and Biotechnology, 2015. **3**(175).
69. PerkinElmer, *Operetta: Operation manual*. 2011, Author: UK.
70. Lawrie, G., et al., *Interactions between Alginate and Chitosan Biopolymers Characterized Using FTIR and XPS.* Biomacromolecules, 2007. **8**(8): p. 2533-2541.

71. Ibrahim, M., et al., *Molecular spectroscopic analyses of gelatin.* Spectrochimica Acta Part A: Molecular and Biomolecular Spectroscopy, 2011. **81**(1): p. 724-729.
72. Kavasi, R.-M., et al., *In Vitro Biocompatibility Assessment of Nano-Hydroxyapatite.* Nanomaterials, 2021. **11**(5): p. 1152.
73. Ouyang, L., et al., *Three-dimensional bioprinting of embryonic stem cells directs highly uniform embryoid body formation.* Biofabrication, 2015. **7**(4): p. 044101.
74. Ouyang, L., et al., *Effect of bioink properties on printability and cell viability for 3D bioplotting of embryonic stem cells.* Biofabrication, 2016. **8**(3): p. 035020.
75. Mondal, A., et al., *Characterization and printability of Sodium alginate -Gelatin hydrogel for bioprinting NSCLC co-culture.* Scientific Reports, 2019. **9**(1): p. 19914.
76. Neufurth, M., et al., *Engineering a morphogenetically active hydrogel for bioprinting of bioartificial tissue derived from human osteoblast-like SaOS-2 cells.* Biomaterials, 2014. **35**(31): p. 8810-8819.
77. Zhang, Z., et al., *Evaluation of bioink printability for bioprinting applications.* Applied Physics Reviews, 2018. **5**(4): p. 041304.
78. Klotz, B.J., et al., *Gelatin-methacryloyl hydrogels: towards biofabrication-based tissue repair.* Trends in biotechnology, 2016. **34**(5): p. 394-407.
79. Giuseppe, M.D., et al., *Mechanical behaviour of alginate-gelatin hydrogels for 3D bioprinting.* Journal of the Mechanical Behavior of Biomedical Materials, 2018. **79**: p. 150-157.
80. Petta, D., et al., *Three-Dimensional Printing of a Tyramine Hyaluronan Derivative with Double Gelation Mechanism for Independent Tuning of Shear Thinning and Postprinting Curing.* ACS Biomaterials Science & Engineering, 2018. **4**(8): p. 3088-3098.
81. Adhikari, J., et al., *Development of hydroxyapatite reinforced alginate–chitosan based printable biomaterial-ink.* Nano-Structures & Nano-Objects, 2021. **25**: p. 100630.
82. Wüst, S., et al., *Tunable hydrogel composite with two-step processing in combination with innovative hardware upgrade for cell-based three-dimensional bioprinting.* Acta Biomaterialia, 2014. **10**(2): p. 630-640.
83. Gao, T., et al., *Optimization of gelatin–alginate composite bioink printability using rheological parameters: a systematic approach.* Biofabrication, 2018. **10**(3): p. 034106.
84. Schwab, A., et al., *Printability and Shape Fidelity of Bioinks in 3D Bioprinting.* Chemical Reviews, 2020. **120**(19): p. 11028-11055.
85. Ji, S. and M. Guvendiren, *Recent Advances in Bioink Design for 3D Bioprinting of Tissues and Organs.* Frontiers in Bioengineering and Biotechnology, 2017. **5**(23).
86. Diloksumpan, P., et al., *Combining multi-scale 3D printing technologies to engineer reinforced hydrogel-ceramic interfaces.* Biofabrication, 2020. **12**(2): p. 025014.
87. Chai, Q., Y. Jiao, and X. Yu, *Hydrogels for Biomedical Applications: Their Characteristics and the Mechanisms behind Them.* Gels, 2017. **3**(1): p. 6.
88. Zuo, Y., et al., *Photo-Cross-Linkable Methacrylated Gelatin and Hydroxyapatite Hybrid Hydrogel for Modularly Engineering Biomimetic Osteon.* ACS Applied Materials & Interfaces, 2015. **7**(19): p. 10386-10394.
89. Zhou, X., et al., *3D Bioprinting a Cell-Laden Bone Matrix for Breast Cancer Metastasis Study.* ACS Applied Materials & Interfaces, 2016. **8**(44): p. 30017-30026.
90. Babaliari, E., G. Petekidis, and M. Chatzinikolaidou, *A Precisely Flow-Controlled Microfluidic System for Enhanced Pre-Osteoblastic Cell Response for Bone Tissue Engineering.* Bioengineering, 2018. **5**(3): p. 66.
91. Chaudhuri, O., et al., *Hydrogels with tunable stress relaxation regulate stem cell fate and activity.* Nature materials, 2016. **15**(3): p. 326-334.